Reynolds Number Effects on Fully-Developed Pulsed Jets Impinging on Flat Surfaces

Medina, H., Benard, E., & Early, J. M. (2013). Reynolds Number Effects on Fully-Developed Pulsed Jets Impinging on Flat Surfaces. AIAA Journal, 51(10), 2305-2318. DOI: 10.2514/1.J051203

Published in:
AIAA Journal

Document Version:
Peer reviewed version

AIAA JOURNAL
Vol. , No. ,

Reynolds Number Effects on Fully Developed Pulsed Jets Impinging on Flat Surfaces

H. Medina*
Coventry University, Coventry, England CV1 5FB, United Kingdom
E. Benard†
Institut Supérieur de l'Aéronautique et de l'Espace, 31055 Toulouse, France
and
J. M. Early‡
Queen's University of Belfast, Belfast, Ireland BT9 5AH, United Kingdom

DOI: 10.2514/1.J051203

A systematic study of the effect of the Reynolds number on the fluid dynamics and turbulence statistics of pulsed jets impinging on a flat surface is presented. It has been suggested that the influence of the Reynolds number may be somewhat different for a jet subjected to pulsation when compared to an equivalent steady jet. A comparative study of both steady and pulsating jets is presented for a Reynolds number range from $Re = 4{,}730$ to $Re = 10{,}000$. All the other factors that affect the flowfield are kept constant, which are $H/d = 3$, $St = 0.25$, and $d = 30.5$ mm. It was found that for the range of the Reynolds numbers tested, pulsation results in a shortening of the jet core, the centerline axial velocity component declines more rapidly, and higher values of the radial velocity component for $r/d > 0.75$ are observed. As the Reynolds number increases, the jet spreads more rapidly, the turbulent kinetic energy and nondimensional turbulent fluctuations decrease, and the flowfield near the impinging surface changes drastically, which is evident with the development of a turbulent momentum exchange interaction away from the wall for $r/d > 1.5$.

Nomenclature

A_N	=	pulse amplitude, $U_{\text{rms}}/U_{\text{avg}}$
d	=	nozzle diameter, m
H	=	nozzle-to-plate spacing, m
K	=	mean turbulent kinetic energy, m^2/s^2
Re	=	Reynolds number, $U_0 d/\nu$
r	=	radial distance measured from the jet centerline, m
St	=	Strouhal number, fd/U_0
T_{avg}	=	average temperature $(T_1 + T_2)/2$, °C
T_r	=	room temperature, °C
T_1	=	experiment start temperature, °C
T_2	=	experiment end temperature, °C
U, V	=	mean axial and radial velocity components, m/s
U_0	=	time-averaged centerline exit velocity, m/s
U', V'	=	mean axial and radial turbulent velocity components, m/s
u, v	=	instantaneous axial and radial velocity components, m/s
x	=	axial distance from nozzle exit, m
$\delta_{1/2}$	=	jet half-width, $r(x, U = U_0/2)$, m
ν	=	kinematic viscosity, m^2/s

I. Introduction

WHEN the development of a freejet flow is interrupted by the presence of a surface, an impinging jet is created. Impinging jets are characterized by a rapid deceleration of the discharged fluid as it reaches the surface, which results in an exchange of momentum between the fluid and the impingement surface that leads to high rates of heat and mass transfer. Consequently, impinging jets have found a place in many industrial applications (for example, the cooling of electronics and inner surfaces of turbine blades).

Because of the numerous practical applications of impinging jets, their study has been mainly focused on understanding their mass, momentum, and heat transfer characteristics [1–4]. However, an understanding of the underlying fluid mechanics behind these types of jet also offers significant benefits to the study of free shear layers and boundary layers. Furthermore, from a numerical modeling perspective, the study of impinging jets can be incorporated into the development of turbulence models as most are tested on flows, which are parallel to the wall and are, therefore, not equipped to deal with flows on which the streamlines change orientation and become perpendicular to the upstream flow. Even though efforts to improve computational models have been made, they are being held back by the lack of detailed experimental data [5], as a large quantity of the research on impinging jets is still directed toward understanding the heat transfer characteristics of impinging jets at the high Reynolds numbers, because they lead to the highest rates of heat transfer.

The study of impinging jets has been further complicated by the numerous configurations that are encountered, which has often led to contradictions in the observations made about their behavior, for instance the value of the nozzle-to-plate spacing, which leads to maximum heat transfer enhancement, can be strongly affected by the upstream turbulence intensity, as well as the type of nozzle employed [6]. There is also a possibility that the use of a pulsating rather than steady jet could enhance the heat transfer rates [7–9], but this has not been conclusively proven. Contradictory evidence exists, which indicates that the pulsation has a detrimental effect on the heat transfer characteristics [7,10,11]. Although these discrepancies in the heat transfer characteristics exist, there is, in addition, a fundamental lack of research on the velocity and turbulent fields of these jet structures. There are only a few works available that study the velocity field of impinging pulsed jets [12,13], but the focus is still firmly on the heat transfer mechanism with limited velocity data presented.

It is, therefore, evident that due to the large number of potential experimental configurations, and the contradictions observed throughout the literature for both steady and pulsating jets, there is

Presented at the 40th AIAA Fluid Dynamics conference and exhibit, Chicago, 28 June 2010; received 31 January 2011; revision received 19 December 2012; accepted for publication 2 April 2013; published online XX epubMonth XXXX.

*Senior Lecturer, Faculty of Engineering and Computing.
†Senior Lecturer, SUPAERO.
‡Lecturer.

a need for both a systematic approach to the study of impinging jets and an in-depth study of the flowfield and fluid mechanics. This will not only serve as a basis to understanding how the velocity field might affect heat transfer but also to provide data for turbulence model validation. The current paper presents the results of an experimental study conducted into the effects of pulsation on the flowfield of a turbulent impinging jet, examining the effects of varying the Reynolds number while keeping the nondimensional frequency (Strouhal number) of the pulsation constant. Zumbrunnen and Aziz [14] estimated analytically a useful boundary-layer renewal Strouhal number of $St = 0.26$ for which heat transfer enhancement would be expected at the impingement surface. Therefore, it was considered reasonable to fix the Strouhal number to $St = 0.25$, as this frequency could lead to heat transfer enhancement. Although the preferred mode Strouhal number for axisymmetric jets has been reported as $St = 0.3$ [15], it is possible to find in the literature which heat transfer enhancement has been observed for pulsing frequencies as low as $St = 0.05$ [9]. The nozzle-to-plate spacing was fixed at $H/d = 3$, as it has been reported to be the minimum distance for observable heat transfer enhancement in pulsed jets [16], but it should be noted that heat transfer enhancement has also been observed for $H/d > 3$ [7]. Ultimately, $H/d = 3$ was chosen as the nominal nozzle-to-plate spacing, as the best laser illumination was achieved in this configuration. Finally, the range of the Reynolds numbers considered in this investigation ($3,900 > Re > 10,000$) was chosen for three main reasons: 1) the flowfield and turbulent characteristics for impinging pulsed jets at $St = 0.25$ have not been reported before, 2) there are limited studies that focus on the flow and turbulent characteristics, and 3) it is a very challenging range in terms of the flow physics that can be observed even for steady jets (for instance the breakdown of the initially stable jet shear layer into turbulent eddies in the form of Kelvin–Helmholtz instabilities, as it will be seen later).

II. Experimental Setup and Procedure

A. Experimental Facility

The experiments were undertaken in a custom-built water facility. This facility operates on a recirculating principle, and it relies on a gravity-fed mechanism to generate the jet. An overhead tank provides the required head, and the water passes through a pulsator (the valve remains fully opened for the steady jet experiments) and the nozzle inlet, before finally exiting at the test section into the main water tank. The excess water from the main tank is collected into a reservoir tank and is pumped back up to the overhead tank in order to maintain a constant water level in the head tank (necessary to keep a steady supply of water to the test section). A schematic of the experimental apparatus can be seen in Fig. 1.

The test section is constructed as a rectangular glass tank (inner dimensions of 605.6 mm wide, 302.8 mm tall, and 300.8 mm long) with a wall thickness of 2 mm (capable of holding approximately 55 liters of water). Glass was a convenient material, because it allows visual access to the test section.

To ensure a fully developed exit profile, a round nozzle ($d_{\text{inner}} = 30.5$ mm) of 50 diameters in length was used. The first 40 diameters (1,220 mm) consist of a straight polyvinyl chloride tube (to prevent rusting and ensure that there is no degradation of the inner wall quality). However, for the last 10 diameters (305 mm) of the nozzle, a sleeve was used to ensure that the inner section of the nozzle remained circular.

A custom-built pulsator was used to provide the required control over the nondimensional frequencies tested. The pulsator consists of a rotating valve, a reduction mechanism, and a driving motor. A PB100 (PN25) chromium-plated brass full-bore valve (diameter 25 mm) was modified, so that it could rotate 360 deg, and, therefore, interrupt the flow of water (generating two pulses per revolution). The duty cycle was estimated to be approximately 50%. The rotating valve was driven using a motor manufactured by ABB (model M2VA71B-2) rated at 0.55 kW of power. This three-phase motor was controlled using a control unit also manufactured by ABB. Once a frequency was selected, it was kept constant within ±0.1 Hz. The maximum frequency at which the motor could be rotated was 47.5 Hz, which translates to a maximum jet frequency of 2.8 Hz for the valve due to the presence of the reduction mechanism.

B. Data Acquisition

A high-speed PIV system was used in order to acquire time-resolved velocity data. This system is comprised of a laser head, a power supply unit, a chiller (used to cool the laser head), a high-speed camera, and a personal computer. Both the laser head and the power supply unit are manufactured by Lightwave Electronics. The laser head consists of a Nd:YAG laser, which produces pulses of a wavelength of 532 nm at a maximum power of 100 mW. The system can be triggered internally and externally; if the system is triggered

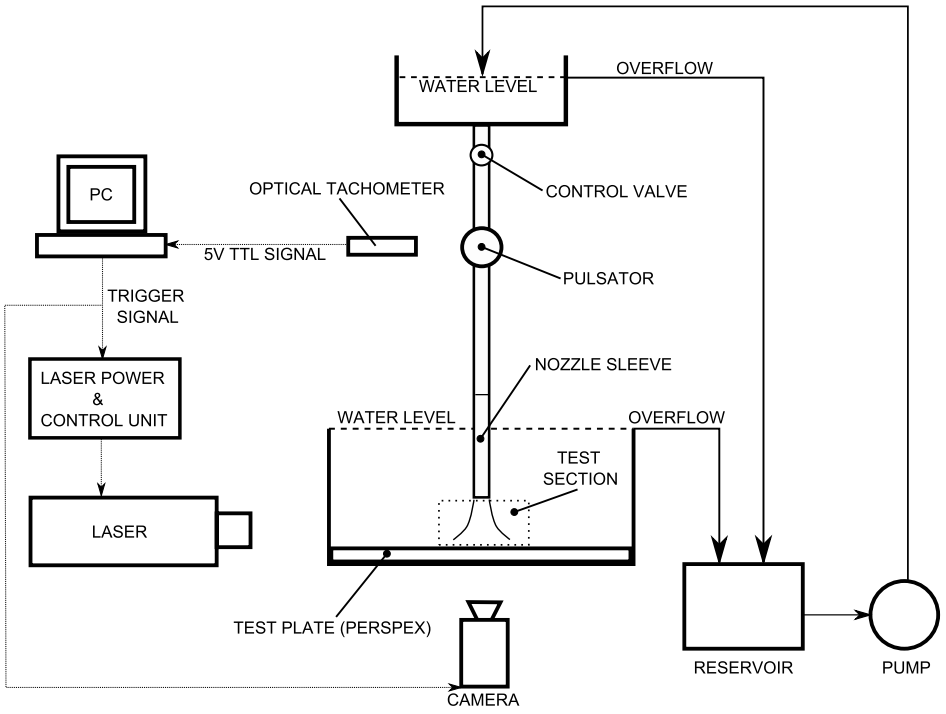

Fig. 1 Experimental facility schematic.

internally, it can be operated at frequencies of up to 100 KHz, and if triggered externally, it can operate up to 16 KHz. To maintain the highest possible camera resolution, the maximum operating frequency chosen was 500 Hz. The camera used to capture the images was a HSS-2 HighSpeedStar video camera system (LaVision). This is a single-frame charge-coupled device digital camera with a storage capacity of 1.28 GB (1022 images at the highest resolution). It has a spatial resolution of 1280 pixels by 1024 pixels. The TTL trigger for the pulsed experiments was provided by an optical sensor (Monarch Instrument, model ROS-5W) pointed at the rotating valve. This sensor is needed, so that the images for the pulsed experiments can be taken at the same point in the cycle with an accuracy of 0.005% of the measured frequency. Finally, the number of cycles for each experiment was determined via a series of convergence tests. However, no fewer than 40 cycles were recorded for any given experiment. This task was carried out in order to minimize data storage requirements. The total number of velocity fields available for each experimental configuration are detailed in Table 4.

1. *Software and Calibration*

The image acquisition and postprocessing was performed using LaVision Davis 7.0. The calibration plate used was a 80×80 mm laminated card, which had a white background with 225 black crosses. The distance between cross centroids was 5 mm. The choice of the interrogation window and postprocessing was the same for all experiments. A multipass (2) decreasing window size algorithm with a 50% overlap was used. The initial interrogation window size was 128×128 pixels, and the final window size was 32×32 pixels. Because of the use of window overlapping, the final spatial resolution is 16 pixels.

2. *System Accuracy, Error, and Experimental Uncertainty*

With the aid of subpixel estimators used in Davis, the PIV system is capable of measuring displacements as small as 0.1 pixel. Therefore, the minimum resolved speed is a function of the camera magnification and the acquisition frequency. Based on the highest acquisition frequency and the largest field of view (FOV) employed, the system accuracy is ± 0.001 m/s. There are many factors that can lead to errors in the calculation of the velocity vectors. These include the choice of particle, out-of-plane motion, high-displacement gradients, laser accuracy, and peak locking. By an appropriate selection of particles (size and density), most of the potential sources of errors can be eliminated or neglected. For the work presented, the diameter of the particles was a concern, because it is smaller than two pixels, therefore increasing the chance of peak locking, so that antipeak locking algorithms were employed. Vectors were calculated using decreasing window sizes and overlapping, significantly reducing (or eliminating) the bias toward small particle displacements in areas with high-velocity gradients. Consequently, it was determined that the main source of error in the velocity calculation originated from the calibration of the camera. The least accurate mapping function for the experiments carried out in this investigation gave a standard deviation of 0.2 pixel. For a 95% confidence level, interrogation windows could be located within ± 0.4 pixel from its measured position. Therefore, for a final interrogation window of 32×32 pixels, the estimated error is $\pm 1.25\%$.

Table 1 Error summary

Experimental quantity	Associated error
Instantaneous velocities (u, v)	$\pm 1.25\%$
Mean velocities (U, V)	$\pm 1.25\%$
Turbulent components (U', V')	$\pm 2.00\%$
Velocity fluctuations (U'_{rms}/U_0, V'_{rms}/U_0)	$\pm 3.00\%$
Reynolds stresses ($U'V'/U_0^2$)	$\pm 4.50\%$
K/U_0^2	$\pm 5.50\%$

Table 1 presents a summary of the estimated error for the various turbulent statistics presented in this work. The number of vector fields available for the estimation of the various turbulent quantities is shown in Table 4. As already mentioned, the accuracy of the velocity measurements was calculated for the most limiting experiment carried out (the highest Reynolds number). Assuming that the timing error between two consecutive image recordings is negligible, and based on a spatial accuracy of ± 0.4 pixel, the system accuracy for velocity measurements is ± 0.001 m/s or better. The error on the instantaneous and time-averaged velocity measurements was estimated at $\pm 1.25\%$.

C. Data Analysis

Once the velocity data were extracted from the acquired images using Davis 7.0, further analysis on the data was performed using MATLAB. The velocity statistics for the steady jet were obtained using the well-known Reynolds decomposition. However, for the pulsed regime, the velocity statistics were obtained using a triple decomposition of the velocity signal [17,18].

1. *Reynolds Decomposition*

The velocity statistics for the steady jet configurations were obtained using the Reynolds decomposition of the velocity signal shown in Eq. (1), where $u_{(x,r)}$ represents the measured velocity at axial location x and radial location r. $U_{(x,r)}$ is the local mean of the velocity signal, and $u'_{(x,r)}$ is the fluctuating part of the velocity component. Furthermore, the turbulent part of the velocity signal can be extracted by rearranging Eq. (1) to obtain Eq. (2). Using this relation, the turbulent statics can be computed at each position (x, r) over the entire data range, N, using the equations shown in table 2, where N is the number of vector fields. Finally, the time between the vector fields corresponds to $1/f$, where f is the acquisition frequency:

$$u_{(x,r)} = U_{(x,r)} + u'_{(x,r)} \tag{1}$$

$$u'_{(x,r)} = u_{(x,r)} - U_{(x,r)} \tag{2}$$

2. *Triple Decomposition*

The velocity signal of pulsed jets was decomposed using a triple decomposition [18,19] shown in Eq. (3), where $u_{(x,r)_t}$ is the instantaneous or measured velocity, $U_{(x,r)}$ is the time-averaged velocity over all of the cycles, $\tilde{U}_{(x,r)_t}$ is the phase-locked-averaged velocity, measured from $U_{(x,r)}$, and finally, $u'_{(x,r)}$ is the turbulent or fluctuating component. In addition, x and r, represent the axial and radial locations in which the velocity signal is extracted, at time t. To reduce computation time, the time-averaged velocity $U_{(x,r)}$ was combined with the phase-locked average velocity $\tilde{U}_{(x,r)_t}$ resulting in $\hat{U}_{(x,r)_t}$. Equation (3) can be rewritten, as shown in Eq. (4), which represents a dual decomposition of the velocity signal. Finally, the turbulent component of the velocity signal can be extracted using Eq. (5). This process is shown graphically in Fig. 2. Therefore, $u'_{(x,r)_t}$ represents the turbulent part of the velocity signal at time t of the cycle

Table 2 Turbulent quantities equations used for steady jets

Statistic type	Equations
Velocity fluctuations	$U'_{rms(x,r)} = \sqrt{\frac{1}{N}\sum_{i=1}^{N}(u_{i(x,r)} - U_{(x,r)})^2}$
Mean TKE	$K_{(x,r)} = \frac{1}{2N}\sum_{i=1}^{N}(u_{i(x,r)} - U_{(x,r)})^2 + (v_{i(x,r)} - V_{(x,r)})^2$
Reynolds shear stress	$U'V'_{(x,r)} = \frac{1}{N}\sum_{i=1}^{N}(u_{i(x,r)} - U_{(x,r)})(v_{i(x,r)} - V_{(x,r)})$

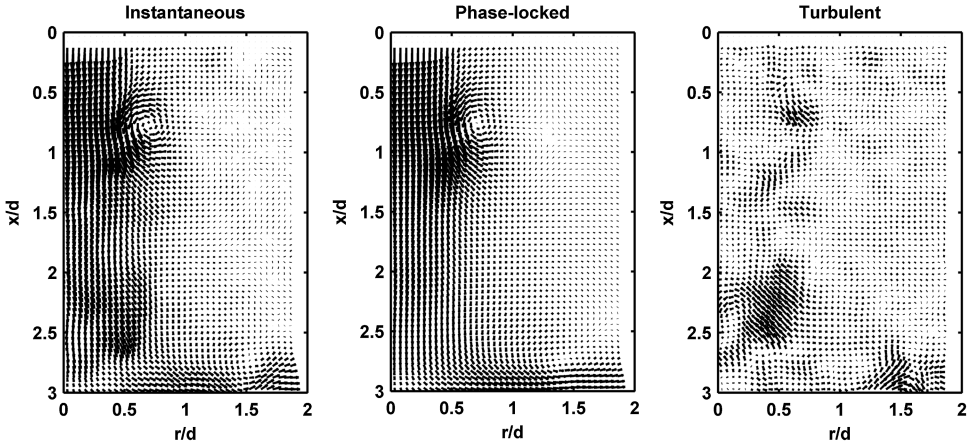

Fig. 2 Decomposition of the velocity signal (whole field) in which the local reference frame data are located at nozzle exit and the jet centerline (i.e., $x/d = 0$ and $r/d = 0$). Only the left-hand side of the jet is shown.

but with the cyclic component removed. The relations used in order to calculate the turbulent quantities for pulsed jets are shown in Table 3, where N is the total number of velocity fields, and t_i represents the time in the cycle that corresponds to a given value of N:

$$u_{(x,r)_t} = U_{(x,r)} + \tilde{U}_{(x,r)_t} + u'_{(x,r)_t} \tag{3}$$

$$u_{(x,r)_t} = \hat{U}_{(x,r)_t} + u'_{(x,r)_t} \tag{4}$$

$$u'_{(x,r)_t} = \hat{U}_{(x,r)_t} - u_{(x,r)_t} \tag{5}$$

D. Test Conditions

The primary aim of the current work is to examine the effect of the Reynolds number on the flowfield of turbulent pulsating impinging jets. All the other parameters that affect the flowfield of pulsating jets were kept constant ($St = 0.25, H/d = 3$, and $d = 30.5$ mm). A detailed summary of the test conditions is given in Table 4.

E. Flow Characterization

A round nozzle was used in order to provide an axisymmetric jet flow with the flow demonstrating a good symmetry apart from at the low Reynolds numbers ($Re < 5,000$), where there was a slight break in symmetry near the impinging wall for $0.6 < r/d < 1.4$, with a maximum deviation of approximately 18%. This break in symmetry is attributed to laser light reflections present in the near wall region on the left-hand side of the FOV, which impaired the calculation of the velocity vectors.

The experimental rig was designed to generate impinging jets with a fully developed exit velocity profile (1/7th power-law velocity distribution). For the steady-flow regime, the velocity profiles at exit were fully developed for the Reynolds numbers greater than 3250. However, for the pulsed flow regime, the exit velocity profiles were only fully developed for the Reynolds numbers greater than 3500. Finally, Fig. 3 has been included in order to provide an overview of the energy content in the spectral domain.

III. Results and Discussion

A. General Characteristics of Impinging Jet Flows

The flow of submerged jets impinging on a flat surface is not only important because of its industrial applications but also due to the various flow features it exhibits (i.e., free shear layer, wall jets, coherent structures, etc.), which are of interest in the study of turbulence. Impinging jet flows can also offer insights for the development of prediction codes and turbulence models. In this section, the main flow regions of a typical jet impinging on a flat plate are introduced (as this information can serve as the basis for characterizing the base flow), and it will also facilitate the comparison of results for the steady and unsteady impinging jets presented in this paper.

Table 3 Turbulent quantities equations used for pulsed jets

Statistic type	Equations
Velocity fluctuations	$U'_{\mathrm{rms}(x,r)} = \sqrt{\frac{1}{N}\sum_{i=1}^{N}(u_{i(x,r)_{t_i}} - \hat{U}_{(x,r)_{t_i}})^2}$
Triple correlations	$U'^3_{(x,r)} = \frac{1}{N}\sum_{i=1}^{N}(u_{i(x,r)_{t_i}} - \hat{U}_{(x,r)_{t_i}})^3$
Mean TKE	$K_{(x,r)} = \frac{1}{2N}\sum_{i=1}^{N}(u_{i(x,r)_{t_i}} - \hat{U}_{(x,r)_{t_i}})^2 + (v_{i(x,r)_{t_i}} - \hat{V}_{(x,r)_{t_i}})^2$
Reynolds shear stress	$U'V'_{(x,r)} = \frac{1}{N}\sum_{i=1}^{N}(u_{i(x,r)_{t_i}} - \hat{U}_{(x,r)_{t_i}})(v_{i(x,r)_{t_i}} - \hat{V}_{(x,r)_{t_i}})$

Table 4 Test conditions summary (velocities in m/s)

Variables			Temperatures, °C				Acquisition information		Exit conditions			
Re	H/d	St	T_r	T_1	T_2	T_{avg}	Frequency, Hz	No. of fields	$U_{\min}$	$U_{\max}$	U_e	A_N
3900	3	— —	19.00	20.00	20.20	20.10	250	3066	— —	— —	0.128	— —
6290	3	— —	19.00	20.10	20.40	20.25	250	3066	— —	— —	0.205	— —
9200	3	— —	21.00	21.40	21.60	21.50	500	3066	— —	— —	0.291	— —
10,120	3	— —	19.00	20.50	20.60	20.55	500	3066	— —	— —	0.330	— —
4730	3	0.25	18.10	19.90	20.30	20.10	125	6825	0.120	0.204	0.155	20%
6000	3	0.25	20.10	23.00	25.50	24.25	250	6498	0.152	0.345	0.178	25%
7820	3	0.25	17.10	16.10	16.90	16.50	250	8520	0.190	0.397	0.2817	25%
10,000	3	0.25	17.90	18.60	19.30	18.95	500	13,284	0.223	0.502	0.3364	30%

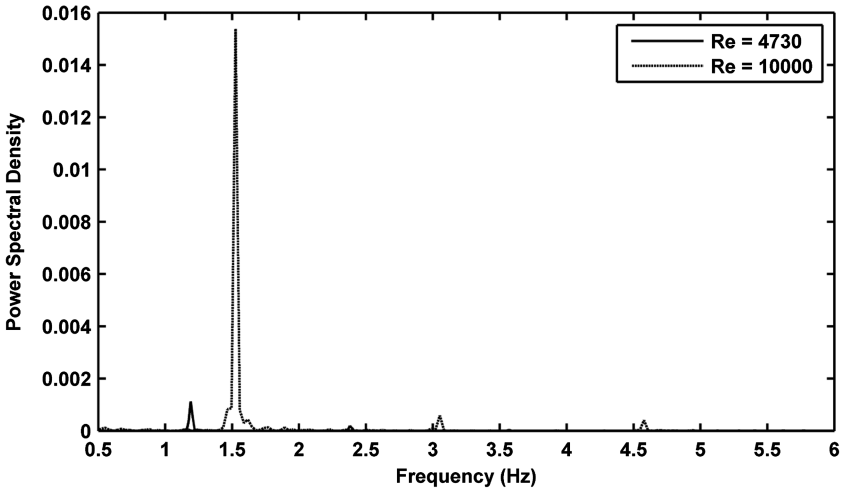

Fig. 3 Power spectral density for the lowest and the highest Reynolds number pulsed jets tested. The power density was calculated at $x/d = 0.1$ and $r/d = 0$.

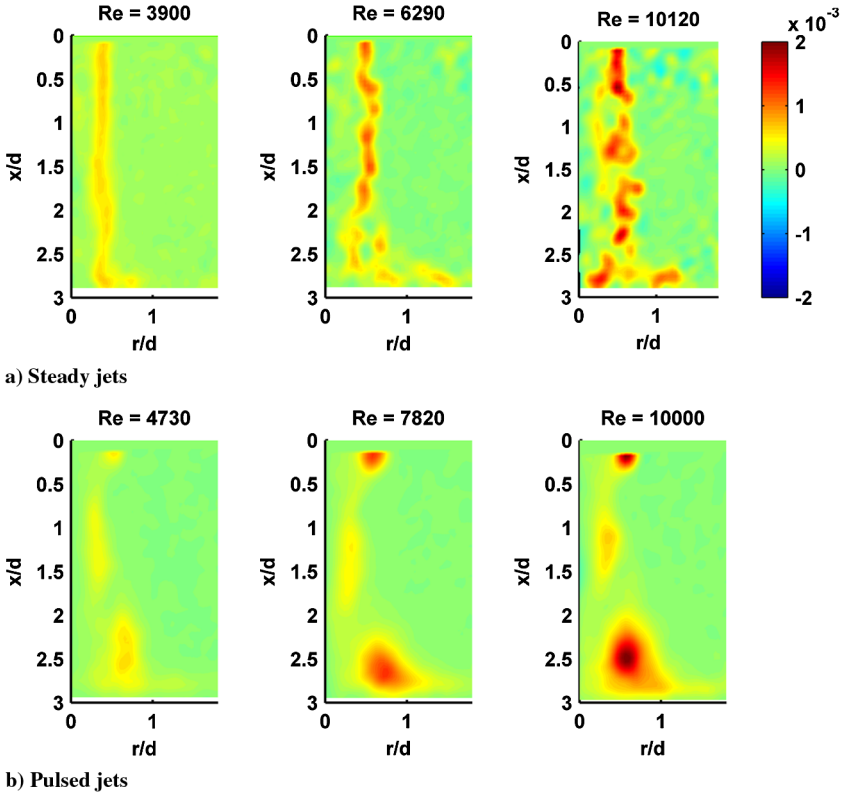

Fig. 4 Effect of the Reynolds number on the dimensionless vorticity ($wd/U^{-}1$, where U is the mean local velocity) field of steady and pulsed impinging jets ($H/d = 3$,$St = 0.25$). The jet exit is located at ($x/d = 0, r/d = 0$), the impingement surface at $x/d = 3$, and the stagnation point at ($x/d = 3, r/d = 0$). The right half of the jet is shown. The same convention will be used in subsequent surface plots.

The flow of an impinging jet is typically characterized by three distinct regions: 1) the potential region, 2) the impinging, decaying, or decelerating region, and 3) the wall jet region. The flow characteristics for each of these regions are clearly distinct from each other.

First, the potential region, if it exists, is developed as the jet exits the nozzle. This region is characterized by very low levels of vorticity (unless the jet is swirling). The velocity profiles in this region are mainly dictated by the nozzle from which the jet is issued. In the case of a round nozzle, the flow develops into a parabolic velocity profile. One of the main characteristics of the potential region is that the initial or exit velocity of the flow is preserved. As the flow travels downstream (i.e., away from the nozzle exit), the cross-sectional area of the potential region reduces, the jet widens, and the axial velocity profile flattens. These effects are a manifestation of the viscous diffusion of momentum. The shear layer forms as a result of the usually large velocity gradient between the jet and the surrounding fluid. In the case of a steady round jet, the shear layer is stable at the low Reynolds numbers, and as the Reynolds number is increased, the shear layer begins to destabilize in the form of Kelvin–Helmholtz instabilities. As the Reynolds number is further increased, these instabilities break down into turbulent eddies (Fig. 4). When the jet is pulsed, this pulsation (at sufficiently large amplitudes) leads to the formation of a vortex ring, which dominates the flow features within the shear layer. The characteristics of these toroidal structures are dictated by the jet configuration (the Reynolds number, Strouhal number, nozzle, etc.). The strength of these vortices (based on their vorticity) is known to increase as both the Reynolds number and the Strouhal number are increased (Fig 4).

As the flow approaches the impingement surface, the impinging region is generated and is characterized by a reduction in axial velocity, which continues to decelerate until the flow reaches the surface and the stagnation region is formed. This flow deceleration in the axial direction is accompanied with an increase in mass and momentum transfer to the impinging surface. At the stagnation point, there is a local increase in pressure, which forces the flow radially outward, leading to the formation of the third flow region, namely, the wall jet region, in which mass and momentum transfer are also significant. At the boundary in which the flow begins to turn, the shear layer is forced radially, and in steady jets with sufficiently large Reynolds numbers, this results in a distortion of turbulent eddies, which is believed to be another mechanism by which heat and mass transfer at the wall can be enhanced [20]. For pulsed jets with well-defined coherent structures within the shear layer, the turbulence characteristics, and, hence, the heat and mass transfer behavior within the wall jet, is known to be strongly dominated by the upstream features of the coherent structures [21] and their interaction with the impingement surface as they are displaced radially outward until they eventually dissipate. In the following sections, those upstream features will be investigated and reported. This work will focus on the flow and turbulent characteristics within the potential and decelerating regions, but some information concerning this wall jet region will also be presented.

B. Time-Averaged Flowfield

Figure 5 exemplifies some of the flow features of the potential and decelerating flow regions described in the preceding section. The mean axial velocity profile at the jet centerline for the steady and pulsating jets considered in this work is shown. At a first glance, it is noticed that the potential region for these jets extends up to $x/d \approx 2$. However, at approximately $x/d > 2$, the presence of the impingement surface results in a deceleration of the flow in the axial direction. In the axial range $0 < x/d < 2$, all pulsed jets exhibit an increase in axial velocity. Furthermore, this increase in centerline velocity becomes more pronounced as the Reynolds number is increased, with the jet at $Re = 10,000$ reaching a maximum velocity of $U/U_0 = 1.07$ at $x/d \approx 1.19$. This localized increase in axial velocity is attributed to a back pressure at the rotating valve due to water hammer effects. A closer evaluation of Fig. 5 shows that for steady jets, there is no significant deceleration of the jet centerline velocity up to $x/d = 2$. In contrast, for pulsating jets, an earlier decline in the jet centerline velocity is observed at $x/d = 1.5$, following on from the initial acceleration. This decay in the centerline axial velocity component becomes evident for $Re = 7,820$ and $Re = 10,000$ (Fig. 5b), indicating that the presence of the pulse shortens the core of the jet as the Reynolds number is increased from $Re = 6,000$ to $Re = 7,820$. However, for steady jets, the Reynolds number does not have a significant effect on the rate of centerline velocity decay at least for the range of the Reynolds numbers tested (i.e., $3,900 < Re < 10,000$).

The effect of the Reynolds number on the development of the axial and radial velocity components is shown in Fig. 6. The Reynolds number does not have a strong influence on the development of the axial velocity component. However, the development of the radial velocity, V/U_0, component is influenced by the Reynolds number (Fig. 6b). For pulsed jets, the lateral acceleration rate of the jet is increased as the jet approaches the impingement region. This is a consequence of an increase in the local pressure near the impingement surface, which forces the jet to accelerate in the radial direction, and the vortex ring is displaced radially away from the jet centerline and stagnation region. However, this effect of the Reynolds number is moderate within the range considered in this work, and it is also marginally more pronounced for pulsed jets. Interestingly, it can be noticed that the presence of a pulsation leads to a widening of the axial velocity profiles as the Reynolds number is increased as is evident by Fig. 7, which also shows a significant increase in the jet half-width (15% or greater) for $Re = 10,000$ when compared to steady jets. This increase in the spreading, or widening, of the jet axial velocity profiles toward the end of the potential region, and with the impinging region, is attributed to the increased momentum diffusion through the molecular viscosity experienced by the vortex rings as they are shed from the nozzle exit and approach the impingement region, in which the vortex pair shows an increase in size and stretches as seen, for example, in Fig. 4b in which the vorticity of pulsed jets shows the vortex as it approaches the impinging wall (The vorticity surface map shows that the vortical structure grows in size as it travels from the nozzle exit toward the impinging surface.)

Interestingly, the most significant influence of the Reynolds number on pulsed jets is found near the impinging wall. First, the presence of a pulsation leads to higher values of the radial velocity component at $r/d > 1.5$ for all jets in comparison to their steady counterpart. This increase in the radial velocity component near the wall for $r/d > 1.5$ develops as the vortex ring is displaced radially away from the jet centerline, and its angular momentum energizes the wall jet. Furthermore, the magnitude of the local maximum is not proportional to the Reynolds number, for instance the jet with $Re = 4,730$ exhibits a local maximum larger than the jet with $Re = 7,820$; however, it increases for $Re = 10,000$, leading to the largest value of V/U_0. This behavior is a consequence of the significant differences to the magnitude of the dimensionless vorticity between vortex rings due to the influence of the Reynolds number. For instance, as the Reynolds number is increased, the vorticity within the vortex rings increases as shown in Fig. 13. Therefore, the Reynolds number affects the magnitude of the vorticity within the vortex ring as it reaches the impingement wall, which influences its interaction with the impingement surface (Fig. 13). For example, for $Re = 4,730$, the vortex is weak (lower vorticity) and does not penetrate the wall jet; however, for $Re = 7,820$, the vortex penetrates the wall jet. Interestingly, as the Reynolds number is further increased to $Re = 10,000$, its vortex is moved away from the wall, as it is forced away by the fluid within the jet core, which exhibited a widening of the axial velocity profiles as the Reynolds number is increased (Figs. 6b and 7). This suggests that axial momentum is forced radially, leading to the development of a stronger wall jet, which prevents the vortex from penetrating the wall as deeply as the jet with $Re = 7,820$. Finally, the presence of the pulsation fixes the location

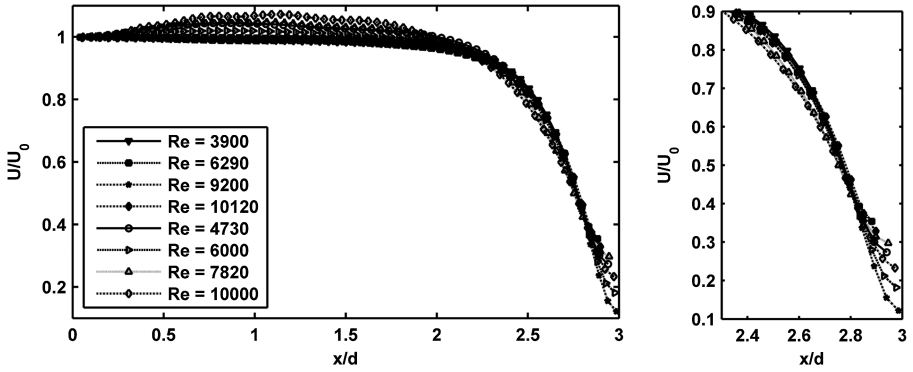

a) $0 < x/d < 3$ b) impingement region close-up

Fig. 5 Centerline axial velocity decay: closed symbols are steady jet, open symbols are pulsed jet ($H/d = 3$,$St = 0.25$).

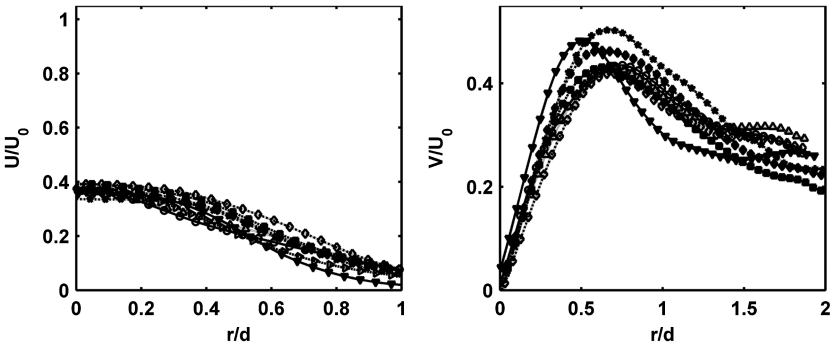

a) x/d = 2.9

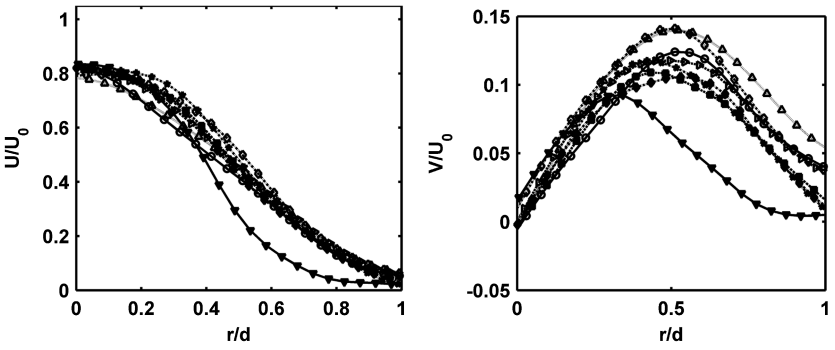

b) x/d = 2.5

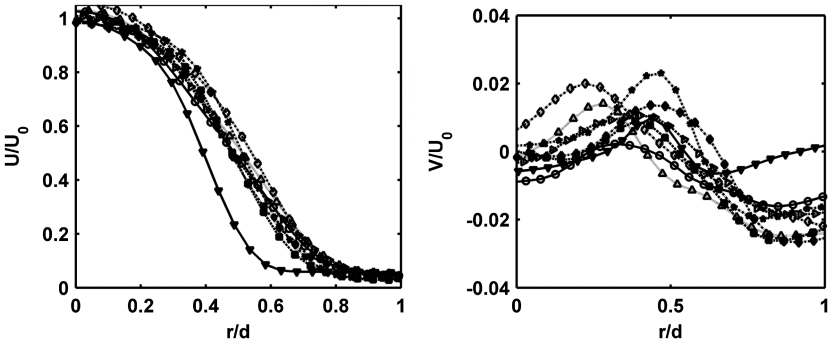

c) x/d = 1.5

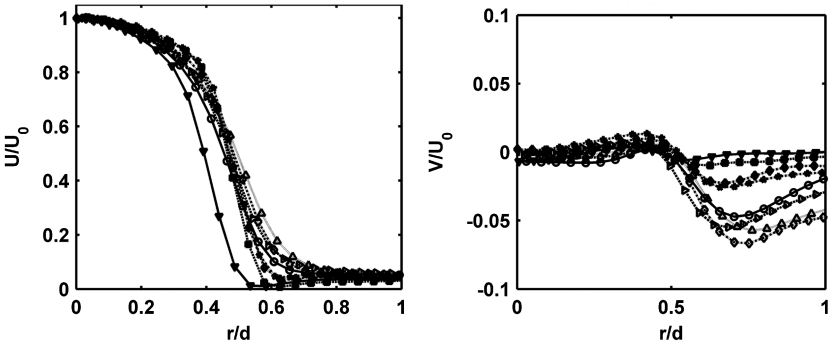

d) x/d = 0.1

Fig. 6 Radial profiles of mean axial (left) and radial (left) velocity components; closed symbols are steady jet, open symbols are pulsed jet ($H/d = 3, St = 0.25$). For a legend, see Fig. 5.

of the maximum radial velocity component near the wall at approximately $r/d = 0.75$, independently of the Reynolds number, at least for the values of the Reynolds number tested. This result suggests that the pulsation has the effect of both controlling the development of the shear layer and fixing the radial location, in which the vortex ring impinges on the surface when $St = 0.25$. This observation deserves further study, as it cannot be generalized unless additional upstream conditions, such as the effect of varying the pulsating frequency or the Strouhal number, are investigated.

C. Velocity Fluctuations

Figure 8 shows that, overall, as the Reynolds number is increased, the nondimensional axial velocity fluctuations decrease. A similar reduction was also encountered in turbulent pulsating jets as the Strouhal number increased [22]. This reduction was due to increased vorticity which helped reduce the turbulent part of the axial velocity component. For the current study, not only does vorticity within the vortex ring increases as the Reynolds number is increased, but the exit velocity also increases, inducing a more pronounced reduction of

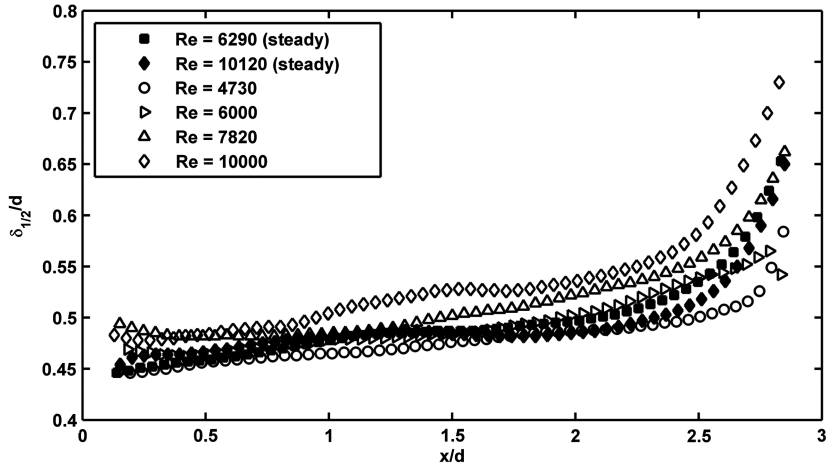

Fig. 7 Axial (streamwise) development of the jet half-width, where $\delta_{1/2} = r(U = U_0/2)$.

$U'_{\rm rms}/U_0$. Similarly, the radial velocity fluctuations (Fig. 8, right) also decrease as the Reynolds number is increased, although this decrease is moderate. Figure 8 shows that near the nozzle exit (Fig. 8d), the profiles of the axial velocity fluctuations for pulsed jets exhibit higher peak values within the jet mixing layer. This increase is linked to the periodic regeneration of the shear layer as a new cycle starts. Similarly, the velocity fluctuations in the radial direction (Fig. 8d, right) show increased values of $U'_{\rm rms}/U_0$ within the shear layer for pulsed jets. Further downstream, at $x/d = 2.5$ (Fig. 8b), the profiles for pulsed jets show an increase of $U'_{\rm rms}/U_0$ for $0 < r/d < 0.25$, and the Reynolds number has a moderate influence on $U'_{\rm rms}/U_0$ at $0.2 < r/d < 0.6$, leading to a decrease in the axial velocity fluctuations when the Reynolds number increases. Furthermore, it is near the impinging wall that the effects of the Reynolds number are most significant as shown in Fig. 8a. It shows that as the Reynolds number is increased, there is a decrease in the values of $U'_{\rm rms}/U_0$. It also shows an increase of $U'_{\rm rms}/U_0$ in comparison to steady jets within the stagnation region ($0 < r/d < 0.3$) as a result of the breakdown of coherent structures near the stagnation region, which also explains the reduction in the values of $U'_{\rm rms}/U_0$ with increasing the Reynolds number (increased vorticity within the vortex pair near the wall).

Figure 8a (right) shows radial profiles of the radial velocity fluctuations near the wall. It can be observed that for $r/d > 1$, the effect of the Reynolds number on $V'_{\rm rms}/U_0$ is similar to that of steady jets; that is, it reduces the value of $V'_{\rm rms}/U_0$. However, for steady jets, this is noticeable from $r/d > 0.5$. This indicates that the presence of the pulse delays the effect of the Reynolds number on $V'_{\rm rms}/U_0$ to $r/d > 0.75$. This reduction in the values of V'/U_0 with increasing the Reynolds number is mostly marked when the Reynolds number increases from $Re = 7,820$ to $Re = 10,000$ (pulsed), and it could be attributed to the development of the wall jet; as the flow impinges on the surface, an area of increased pressure builds up (stagnation region) and as the flow velocity is increased (i.e., $Re = 7,820$ to $Re = 10,000$), the magnitude of the stagnation pressure residual $(\partial P/\rho\partial x)$ calculated from the mean axial momentum balance near the impingement wall [5] increases from approximately 75 N/kg to 200 N/kg. The flow is then forced radially, and the wall jet is formed. With increasing the Reynolds number and the subsequent increase in pressure in the stagnation region, a favorable pressure gradient is present, which stabilizes the wall jet boundary layer due to a localized flow acceleration that increases as the Reynolds number is increased. In the case of a pulsed jet, this radial acceleration effect is less marked due to magnitude reductions of the stagnation pressure residual $(\partial P/\rho\partial x)$ of up to 78% when compared to steady jets. This reduction in the stagnation pressure could be a result of the loss of upstream axial momentum to viscosity. It has already been shown (Figs. 5 and 6) that the potential core of pulsed jets is shorter than that of steady jets. This behavior could contribute to the reduction in stagnation point heat transfer rates often reported in the literature [6] for pulsed or pulsating jets.

Figure 9 shows that there is a steady increase of the centerline velocity fluctuations at $1.25 < x/d < 2.4$ for pulsed jets up to $r/d \approx 2.4$, in which pulsed jets reach higher values of $U'_{\rm rms}/U_0$ than steady jets. In addition, for pulsed jets, the centerline axial velocity fluctuations near the stagnation point decrease as the Reynolds number is increased. This reduction is also observed in steady jets tested; however, it is more pronounced on pulsed jets. Figure 9 also shows that for approximately $x/d < 0.5$, the pulsed jets exhibit increased levels of $U'_{\rm rms}/U_0$, which has been attributed to the cyclic nature of the flow.

D. Turbulent Kinetic Energy

Figure 10 shows that, overall, as the Reynolds number is increased, the mean turbulent kinetic energy (TKE) decreases, particularly within the shear layer of the jet (at $1 < x/d < 2.5$). This effect is due to the decrease of the axial and radial velocity fluctuations as the Reynolds number is increased as a result of increased vorticity within the vortex ring (Figs. 4b and 13), which suggests that at higher values of the Reynolds number, the vortex ring is capable of preserving the angular momentum more effectively, thus preventing an early breakdown of the vortex pairs, and it manifests as a reduction in the values of K/U_0^2 until, eventually, the vortex ring is close to the impingement plate, in which the angular momentum dissipates, and increased TKE is observed. Interestingly, the TKE within the mixing layer of pulsed jets exhibits increased levels of TKE when compared to steady jets, showing that the coherent structures carry a large proportion of the TKE, which is contained within the mixing layer. This energy is then released onto the impingement surface. This behavior suggests that, given an appropriate understanding of the factors influencing this mechanism (e.g., the Strouhal number, nozzle-to-plate-spacing, etc.), pulsed jets have great potential for applications, in which the amount of energy released onto the surface needs to be controlled.

The effect of the Reynolds number near the impinging wall is explored in Fig. 11. For steady jets at $0.6 < r/d < 1.5$, increasing the Reynolds number results in a decrease of the mean TKE. However, there is not a clear correlation for pulsed jets at $0.6 < r/d < 1.5$, although there is a steady increase of the mean TKE for $r/d > 0.9$, whereas for steady jets, this increase is not evident up to approximately $r/d > 1.5$. Finally, for $Re = 7,820$, there is an increase in the values of K/U_e^2 for approximately $0.4 < r/d < 0.9$ when compared to the other jets. This local increase is influenced by the higher values of the radial velocity fluctuations also present at $0.4 < r/d < 0.9$ (Fig. 8). The increase in the values of $V'_{\rm rms}/U_0$ for this region is a result of vortex distortion near the impingement plate as can be seen in Fig. 13, in which the phase-averaged vorticity field for $Re = 7,820$ shows a deformation of the vortex core (compared with $Re = 10,000$ in Fig. 13, in which the vortex ring has retained its upstream shape) combined with the fact that the jet vortex exhibits higher vorticity near the wall and, therefore, has a more pronounced effect on the development of the wall jet.

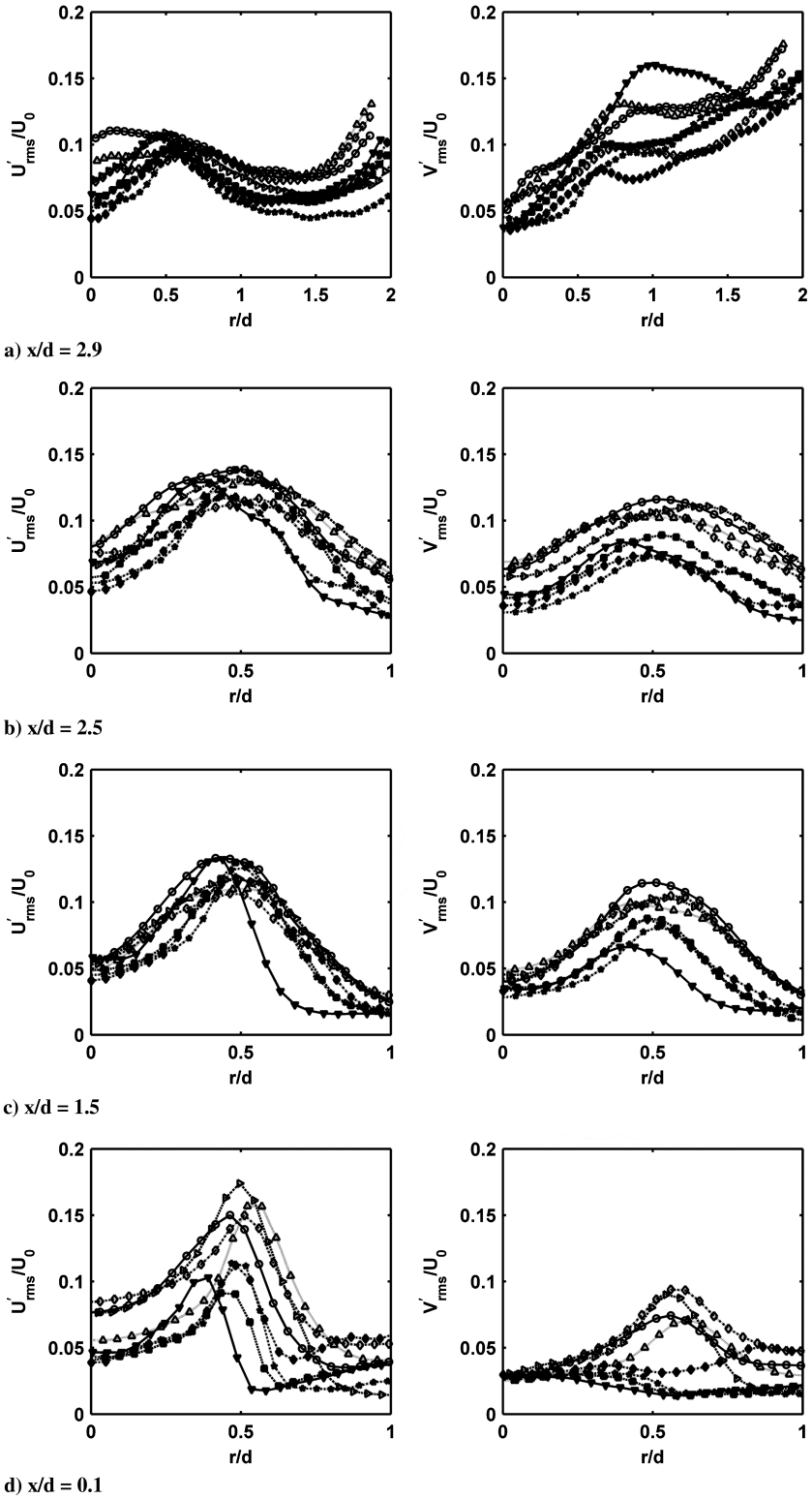

Fig. 8 Radial profiles of mean axial (left) and radial (left) velocity fluctuations: closed symbols are steady jet, open symbols are pulsed jet ($H/d = 3, St = 0.25$). For a legend, see Fig. 9.

E. Reynolds Shear Stress

It has already been established that the presence of a pulsing frequency has significant effects on the flow of impinging jets. Additionally, the Reynolds number has been seen to influence the flowfield and the turbulent characteristics of impinging jets; noticeably, the presence of a pulsating frequency has been shown to affect the development of the jet's mixing layer, in general, leading to a thicker shear layer with flattened radial profiles when compared to the impinging jets without a pulsing frequency. In this section, we will briefly discuss the effect that the Reynolds number and the presence of a pulsing frequency have on the turbulent stresses. Figure 12 shows radial profiles of the axial, normal, and shear stresses estimated in the two-dimensional FOV available. The main motivation to include these profiles is to provide high-quality and detailed estimations of the distribution of the Reynolds stresses for the pulsating jet flows. The Reynolds stresses are, perhaps, one of the most desirable turbulent quantities to investigate. The distribution of the Reynolds stresses can provide information on the effects that

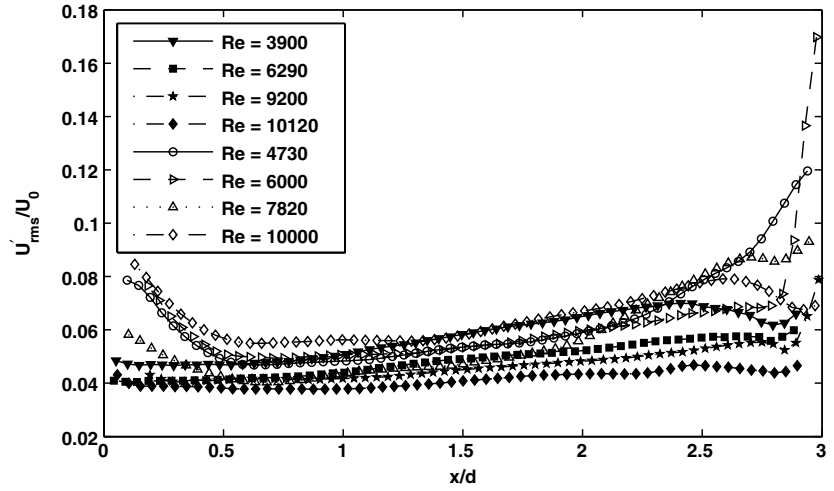

Fig. 9 Effect of the Reynolds number on the centerline axial velocity fluctuations: closed symbols are steady jet, open symbols are pulsed jet ($H/d = 3$,$St = 0.25$).

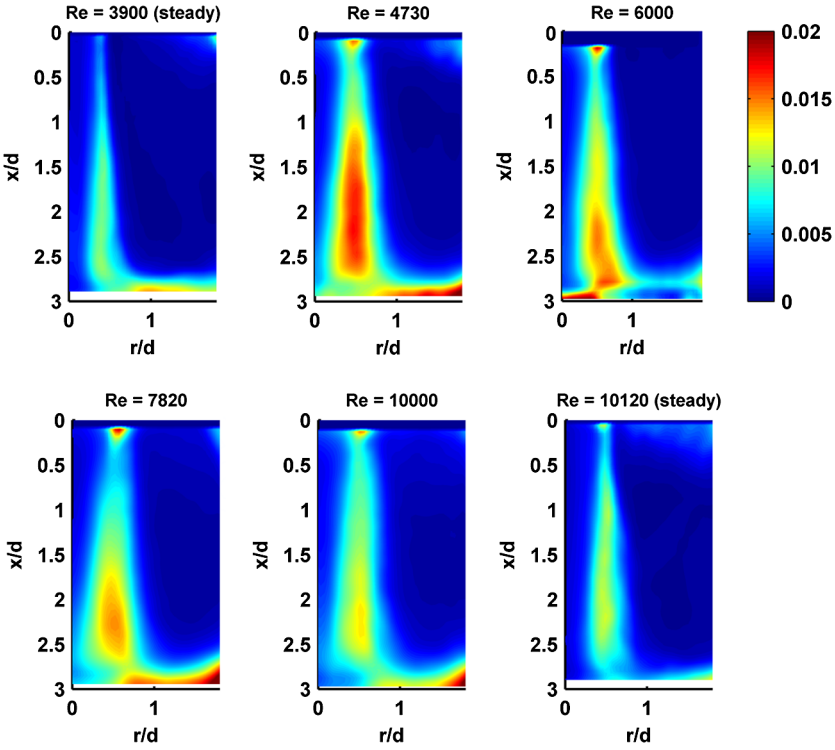

Fig. 10 Effect of the Reynolds number on the mean TKE K/U_0^2 ($H/d = 3$, $St = 0.25$).

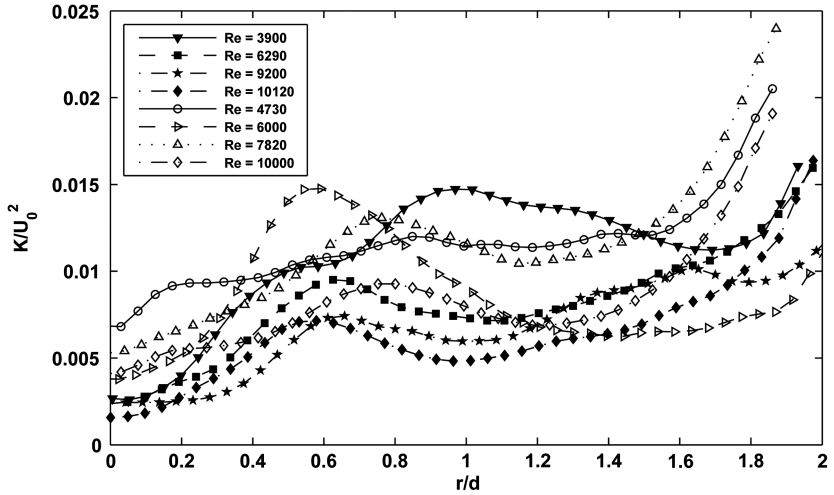

Fig. 11 Effect of the Reynolds number on the mean TKE near the impinging wall: closed symbols are steady jet, open symbols are pulsed jet ($H/d = 3$, $St = 0.25$, $x/d = 2.85$).

turbulence has on many flows, because they are considered as one of the most influential mechanisms for the transport of turbulent momentum. It is not surprising to find that many analytical and numerical tools are based on or rely on the modeling and/or mimicking the effect that small-scale velocity fluctuations have on the mean flow and the instantaneous flowfield. Furthermore, these small scales (in comparison to the mean flow scales) can also have a marked effect on the transport of passive scalars and can, therefore, significantly affect heat transfer [23]. In this work, every possible effort was make to systematically present the turbulent characteristics of pulsating impinging jets and provide detailed experimental data that can be used in support of numerical and/or theoretical investigations.

In Fig. 12, the left column depicts the distribution of the radial profiles of the axial normal stress. As expected from the discussion in Sec. IV., it is reasonable to foresee peaks in the axial normal stress concentrating toward the mixing layer, because within this layer there is a net momentum transfer from the issuing jet to the surrounding fluid. Furthermore, considering that so far the distributions of turbulent quantities for pulsed jets have followed a similar profile to those of steady jets, it is not surprising to observe a similar pattern emerging. That is, overall, the distribution of turbulent quantities for pulsating jets have a tendency to exhibit flatter distributions within the shear layer of the jet with similar magnitudes to those generated by steady jets, particularly for $1 < x/d < 2.5$. However, Fig. 12d (left) shows that near the nozzle exit, the normal stress in the axial direction for pulsed jets shows significantly higher peak values. This result can be expected, because it has already been shown that the pulsed jet had wider exit velocity profiles, therefore suggesting an increase of momentum diffusion in the axial direction, which is reflected in the distribution of the normal stresses near the nozzle exit. Similarly, overall the profiles of the radial normal stress for pulsed jets exhibit significantly larger peaks than those observed for steady jets. These results imply that there is an increased turbulent momentum transfer in the radial direction for pulsed jets (Fig. 12). This momentum exchange is controlled and dominated by the large coherent structures emanating from the nozzle exit. Also, near the nozzle exit, the radial velocity maxima generally increase with increasing the Reynolds number.

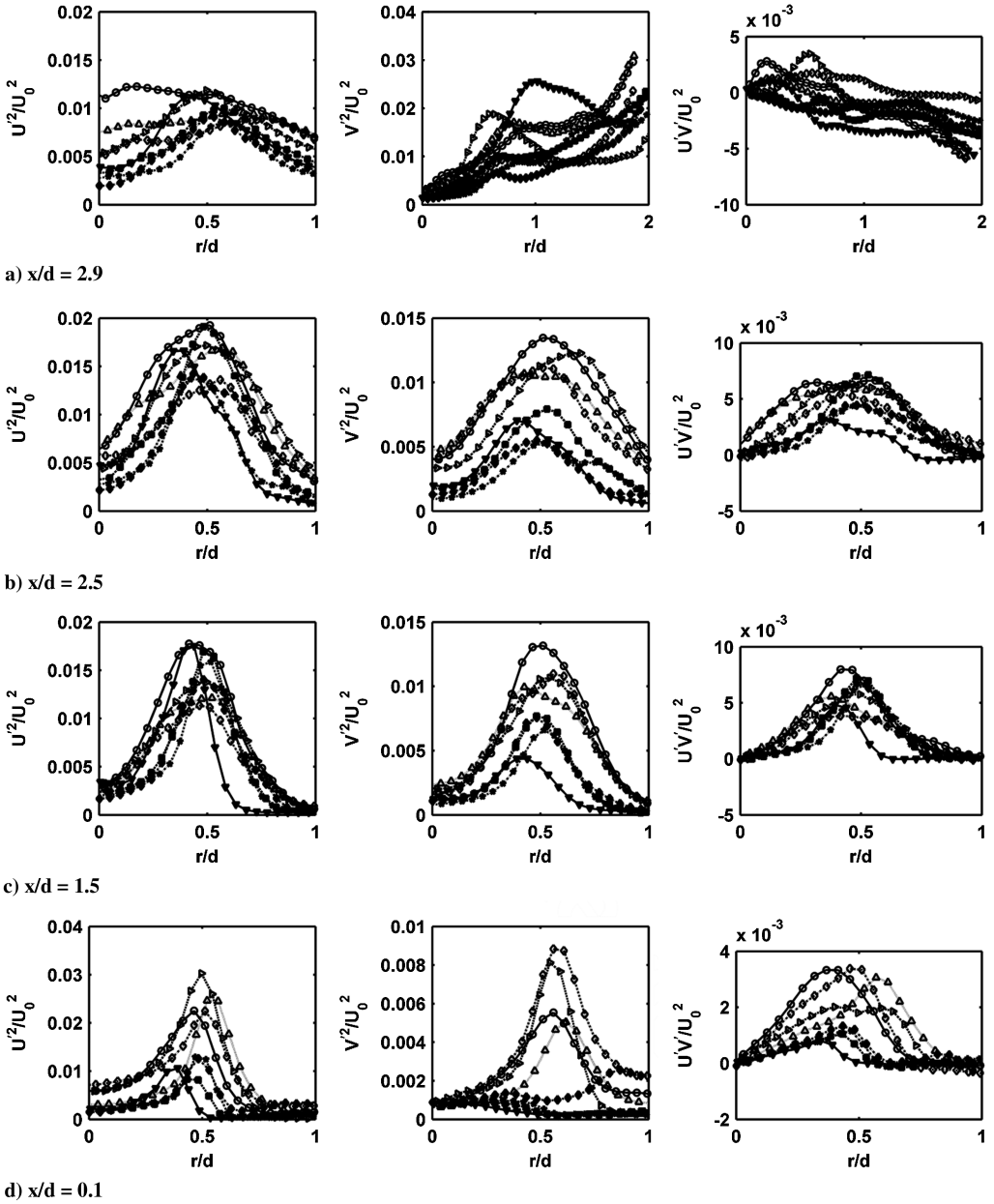

Fig. 12 Radial profiles of the axial normal stress (left), the radial normal stress (center), and the shear stress (right): closed symbols are steady jet, open symbols are pulsed jet ($H/d = 3$, $St = 0.25$). For a legend see Fig. 11.

F. Unsteady Vorticity and Shear Stress

Figure 13 shows the phase-locked vorticity fields at various phase angles within a pulsing cycle. This figure shows that the Reynolds number has a significant effect on the vorticity field of an impinging pulsed jet. The most noticeable effect is that as the Reynolds number is increased, the vorticity within the vortex ring also increases (Fig. 13). This figure also shows a basic characteristic of the flow of impinging toroidal structures. They emanate from the nozzle with a given "strength" or characteristic vorticity and are carried toward the impinging surface by the jet's momentum. As they travel toward the wall, they experience viscous diffusion and, as a result, they lose rotational strength, grow in size (similar to the spread of a freejet due to the viscous loss of momentum), and diffuse until eventually they dissipate into small-scale turbulent structures. Interestingly, Fig. 13 shows that the eventual dissipation of these toroidal structures is strongly influenced by the Reynolds number. As the Reynolds number is increased, the vortex ring exhibits larger upstream vorticity as it develops (Fig. 13) and can, therefore, "survive" or preserve its rotational motion and travel larger distances before it also eventually dissipates. As a result, the vortex distribution near the impinging surface is noticeably affected by the Reynolds number, which could explain the uncorrelated distributions of U'_{rms}/U_0 at the jet centerline near the impingement wall seen in Fig. 9.

Finally, the unsteady (phase-locked) development of the shear stress of three pulsating impinging jets ($Re = 4,730$, $Re = 7,820$, and $Re = 10,000$) is shown in Fig. 14. The phase-locked temporal flowfields presented in Fig. 14 were estimated by first computing the phase-locked (or phase-averaged) velocity over a number of samples. A minimum of 40 cycles was used for $Re = 4,730$, and a maximum of 80 cycles when $Re = 10,000$. The number of samples is not large enough to provide a very smooth shear stress field; however, by first referring to the vorticity field (Fig. 13), some general observations about the flow, as well as the spatial development of the shear stress, can be made. The reader is informed that these two plots (Figs. 13 and 14) have been prepared in such a way that if superimposed, the phase angle and Reynolds number of each figure will be identical. For instance, Fig. 13c (right) shows that at phase angle 25 deg and a jet Reynolds number of 10,000, there is a distorted vortex near the impingement surface at approximately $r/d = 1$. By evaluating the same plot in Fig. 14c, it is possible to observe that near the impingement wall at approximately $r/d = 1$, there is a large region of negative values of $U'V'/U_0^2$. Now considering that our reference frame has its origin at the nozzle exit, and it is positive pointing toward the impingement wall, with the x axis being positive from left to right, it is possible to deduce that in order for the product $U'V'$ to be negative, there are two possibilities: 1) $U' > 0$ and $V' < 0$ or 2) $U' < 0$ and $V' > 0$. This implies that at this location there is an interchange of turbulent momentum from the vortex as it travels along the impinging surface with a "directionality" that is either pointing to the wall and the jet centerline or is away from the impinging surface and the jet centerline. Wallace et al. [24] identified these turbulent momentum transfer interaction as low-speed wall-directed interaction and high-speed outward interactions.

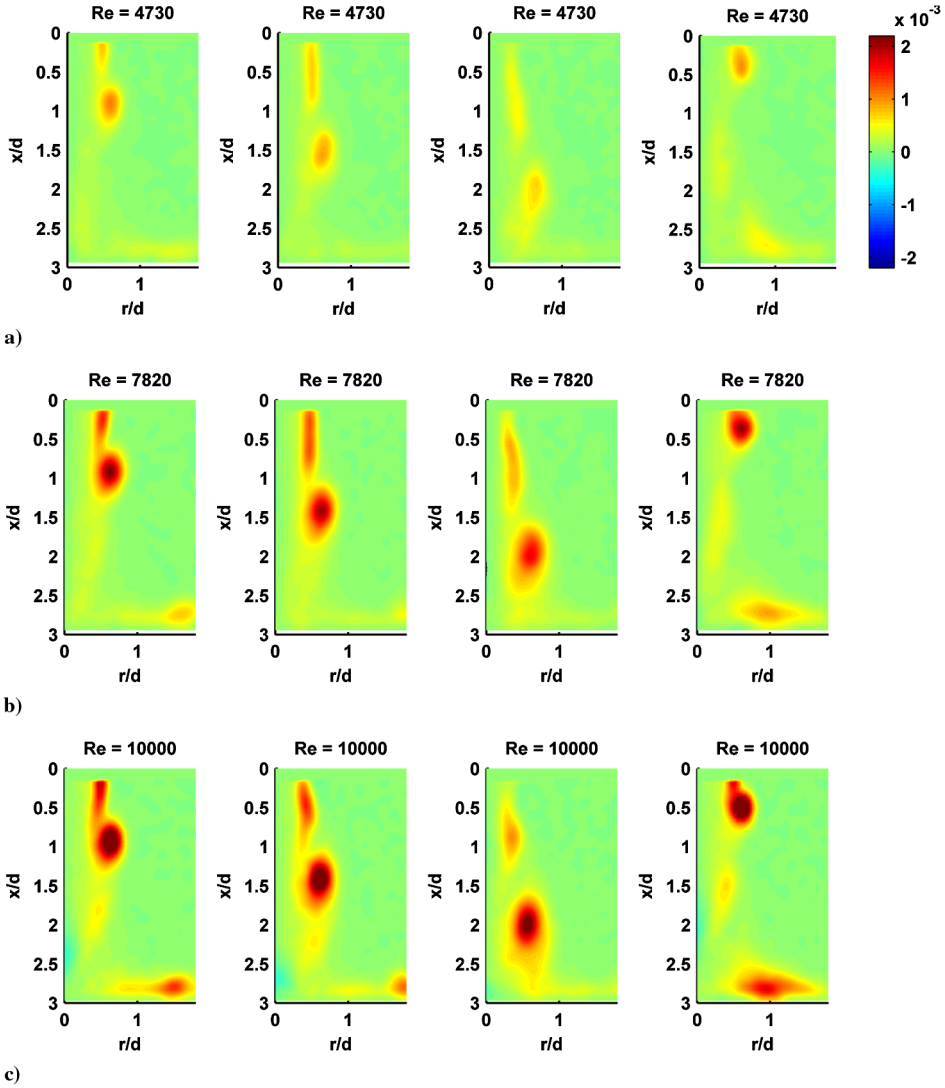

Fig. 13 Phased-averaged dimensionless vorticity at various phase angles: 105 deg, 195 deg, 275 deg, and 25 deg (from left to right). All figures show the dimensionless vorticity ($\omega.d/U^{-1}$) and share the same color map (shown at the top right).

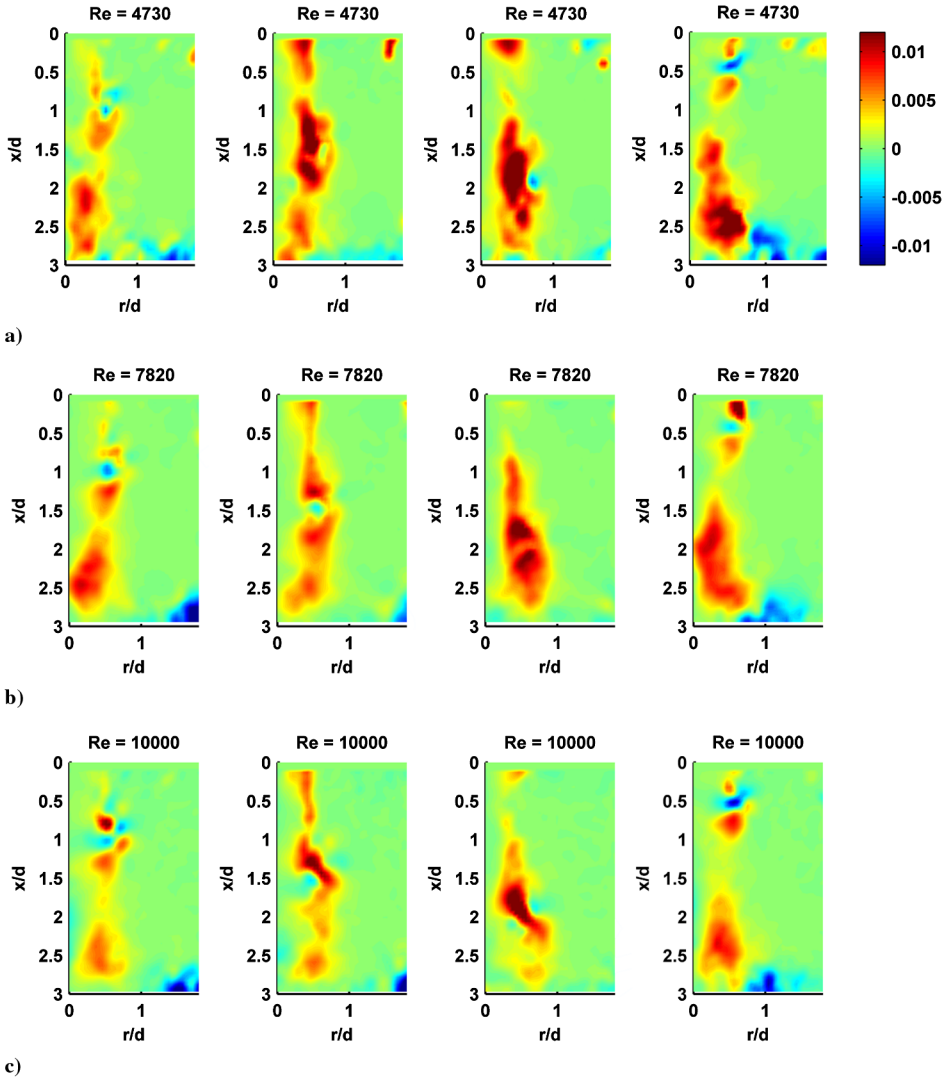

Fig. 14 Phased-averaged dimensionless Reynolds number shear stress at various phase angles: 105 deg, 195 deg, 275 deg and 25 deg (from left to right). All figures show the dimensionless shear stress $U'V'/U_0^2$ and share the same color map (shown at the top right).

Figures 14a and 14b also show that these turbulent momentum exchange interactions between the vortex ring and the wall are influenced by the Reynolds number. As the Reynolds number is increased, the relative strength of these interactions increased, and they also move closer to the wall. These results certainly would seem to support the possibility of employing pulsating impinging jets in applications in which it is desirable to control this turbulent momentum transfer interaction.

IV. Conclusions

The Reynolds number has a significant effect on the flowfield of impinging jets. First of all, for pulsed jets, the jet core shortens, and the centerline axial velocity component declines more rapidly. Also, as the Reynolds number increases, the jet radial velocities within the wall jet increase. This is the case for both pulsed and steady jets. However, this effect is more pronounced for steady jets. Additionally, the presence of a pulsation leads to a widening of the axial velocity profiles in comparison to steady jets. Finally, the presence of the pulsation leads to higher values of the radial velocity component for $r/d > 0.75$ for all of the values of the Reynolds number tested in comparison to the steady cases. However, the results also indicate that the magnitude of the radial velocity near the impingement wall is not in direct relation to the value of the Reynolds number and deserves further consideration.

For pulsed jets, the Reynolds number affects upstream vorticity within the vortex ring and its interaction with the impinging surface. This interaction is not linear with respect to the Reynolds number. For instance, for $Re = 10,000$, the vortex is moved away from the wall, as it is forced away from the wall by the larger exit velocity and subsequent increase in mass flow within the jet core. Therefore, the vortex ring moves radially sooner and more rapidly. This generates a stronger wall jet, which prevents the vortex from penetrating the wall jet as deeply as the jet with $Re = 7,820$. This behavior deserves further study. Finally, an interesting observation is that the presence of a pulse has the effect to fix the location of the maximum radial velocity component near the impinging wall at approximately $r/d = 0.75$. This behavior is independent of the Reynolds number, at least for the values tested.

Increasing the Reynolds number generally decreases the nondimensional turbulent fluctuations U'_{rms}/U_0 and V'_{rms}/U_0. However, the centerline axial velocity fluctuations steadily increase at $1.25 < x/d < 2.4$ for pulsed jets, up to $x/d \approx 2.4$, where pulsed jets develop higher values of U'_{rms}/U_0. This trend is also seen for the mean turbulent kinetic energy (TKE). This increase in both quantities could explain the reduction in heat transfer rates at the stagnation point observed in the literature for pulsed jets. This increase suggests an increase in turbulent mixing, leading to the loss in the jet's original properties in the surrounding fluid. However, the results also show a decrease in turbulent mixing for $0.2 < r/d < 0.6$, corresponding to the wider shear layer seen in pulsed jets. This reduction in U'_{rms}/U_0 within the shear layer, combined with the increase in radial velocity and TKE near the impinging wall, could also explain the heat transfer enhancement observed for pulsed jets away from the stagnation

region. This notion is strengthened further by the development of a turbulent momentum exchange away from the impinging wall for $r/d > 1.5$ as the Reynolds number is increased. This investigation also supports the potential use of pulsating impinging jets in applications, in which there is a need to have control over the turbulent momentum exchange between the jet flow and a flat surface.

References

[1] Ma, C. F., Zheng, Q., Lee, S. C., and Gomi, T., "Impingement Heat Transfer and Recovery Effect with Submerged Jets of Large Prandtl Number Liquid—I. Unconfined Circular Jets," *International Journal of Heat and Mass Transfer*, Vol. 40, No. 6, 1997, pp. 1481–1490. doi:10.1016/S0017-9310(96)00069-5

[2] Ashforth-Frost, S., Jambunathan, K., Whitney, C. F., and Ball, S. J., "Heat Transfer From a Flat Plate to a Turbulent Axisymmetric Impinging Jet," *Proceedings of the Institution of Mechanical Engineers, Part C: Journal of Mechanical Engineering Science*, Vol. 211, No. 2, 1997, pp. 167–172. doi:10.1243/0954406971521746

[3] Moreno, O. A., Katyl, R. H., Jones, J. D., and Moschak, P. A., "Mass Transfer of an Impinging Jet Confined Between Parallel Plates," *IBM Journal of Research and Development* , Vol. 37, No. 2, 1993, pp. 143–155. doi:10.1147/rd.372.0143

[4] Baydar, E., and Ozmen, Y., "An Experimental and Numerical Investigation on a Confined Impinging Air Jet at High Reynolds Numbers," *Applied Thermal Engineering*, Vol. 25, 2005, pp. 409–421. doi:10.1016/j.applthermaleng.2004.05.016

[5] Nishino, K., Samada, M., Kasuya, K., and Torii, K., "Turbulence Statistics in the Stagnation Region of an Axisymmetric Impinging Jet Flow," *International Journal of Heat and Fluid Flow*, Vol. 17, 1996, pp. 193–201. doi:10.1016/0142-727X(96)00040-9

[6] Jamabunathan, K., Lai, E., Moss, M. A., and Button, B. L., "A Review of Heat Transfer Data for Single Circular Jet Impingement," *International Journal of Heat and Fluid Flow*, Vol. 13, No. 2, June 1992, pp. 106–115. doi:10.1016/0142-727X(92)90017-4

[7] Sailor, D. J., Rohli, D. J., and Fu, Q., "Effect of Variable Duty Cycle Flow Pulsations on the Heat Transfer Enhancement for an Impinging Air Jet," *International Journal of Heat and Fluid Flow*, Vol. 20, 1999, pp. 574–580. doi:10.1016/S0142-727X(99)00055-7

[8] Tesar, V., "Enhancing Impinging Jet Heat or Mass Transfer by Fluidically Generated Flow Pulsation," *Chemical Engineering Research and Design*, 2008, pp. 181–192.

[9] Xu, P., Yu, B., Qiu, S., Poh, H. J., and Mujumdar, A. S., "Turbulent Impinging Jet Heat Transfer Enhancement due to Intermittent Pulsation," *International Journal of Thermal Sciences*, 2010, pp. 1–6. doi:10.1016/j.ijthermalsci.2010.01.020

[10] Mladin, E. C., and Zumbrunnen, D. A., "Local Convective Heat Transfer to Submerged Pulsating Jets," *International Journal of Heat and Mass Transfer*, Vol. 40, No. 14, 1997, pp. 3305–3321. doi:10.1016/S0017-9310(96)00380-8

[11] Zvirin, Y., "Heat Transfer Between a Pulsating Impinging Jet and a Flat Surface," *Israel Journal of Technology*, Vol. 5, Nos. 1–2, 1967, pp. 152–169.

[12] Poh, H. J., Kumar, K., and Mujumdar, A. S., "Heat Transfer From a Pulsed Laminar Impinging Jet," *International Communications in Heat and Mass Transfer*, Vol. 32, 2005, pp. 1317–1324. doi:10.1016/j.icheatmasstransfer.2005.07.012

[13] Vejrazka, J., Experimental Study of a Pulsating Round Impinging Jet (Etude Experimentale D'un Jet Circulaire Impactant Pulsant), Ph.D. Thesis, Laboratoire Des Ecoulements Geophysiques Et Industriels, Grenoble, France, Dec. 2002.

[14] Zumbrunnen, D., and Aziz, M., "Convective heat Transfer Enhancement due to Intermittency in an Impinging Jet," *Journal of Heat Transfer*, 1993, pp. 91–98. doi:10.1115/1.2910675

[15] Hussain, A. K. M. F., and Zaman, K. B. Q., "The 'Preferred Mode' of the Axisymmetric Jet," *Journal of Fluid Mechanics*, Vol. 110, 1981, pp. 39–71. doi:10.1017/S0022112081000608

[16] Liu, T., and Sullivan, J. P., "Heat Transfer and Flow Structures in an Excited Circular Impinging Jet," *International Journal of Heat and Mass Transfer*, No. 17, 1996, pp. 3695–3706. doi:10.1016/0017-9310(96)00027-0

[17] Zaman, K. B. M. Q., and Hussain, A. K. M. F., "Vortex Pairing in a Circular Jet Under Controlled Excitation. Part 1. General Jet Response," *Journal of Fluid Mechanics*, Vol. 101, No. 3, 1980, pp. 449–491. doi:10.1017/S0022112080001760

[18] Bremhorst, K., and Gehrke, P. J., "Measured Reynolds Stress Distributions and Energy Budgets of a Fully Pulsed Round Air Jet," *Experiments in Fluids*, Vol. 28, 2000, pp. 519–531. doi:10.1007/s003480050413

[19] Hussain, A. K. M. F., and Zaman, K. B. M. Q., "Vortex Pairing in Circular Jet Under Controlled Excitation. Part 2. Coherent Structure Dynamics," *Journal of Fluid Mechanics*, Vol. 101, No. 3, 1980, pp. 493–544. doi:10.1017/S0022112080001772

[20] Hadžiabdić, M., and Hanjalić, K., "Vortical Structures and Heat Transfer in a Round Impinging Jet," *Journal of Fluid Mechanics*, 2008, pp. 221–260. doi:10.1017/S002211200700955X

[21] Chung, Y. M., Luo, K. H., and Sandham, N. D., "Numerical Study of Momentum and Heat Transfer in Unsteady Impinging Jets," *International Journal of Heat and Fluid Flow*, 2002, pp. 592–600. doi:10.1016/S0142-727X(02)00155-8

[22] Medina, H., Benard, E., Huang, J., and Raghunathan, S., "Study of the Fluid Mechanics of Transitional Steady and Pulsed Impinging Jets Using A High-Speed PIV System," AIAA Paper 2008-766, Jan. 2008.

[23] Gardon, R., and Akfirat, J. C., "The Role of Turbulence in Determining the Heat Transfer Characteristics of Impinging Jets," *International Journal of Heat and Mass Transfer*, Vol. 8, 1965, pp. 1261–1272. doi:10.1016/0017-9310(65)90054-2

[24] Wallace, J. M., Eckelmann, H., and Brodkey, R. S., "The Wall Region in Turbulent Shear Flow," *Journal of Fluid Mechanics*, Vol. 54, No. 1, 1972, pp. 39–48. doi:10.1017/S0022112072000515

F. Alvi
Associate Editor